Front. Earth Sci. 2025, 19(4): 550−565
https://doi.org/10.1007/s11707-025-1164-z

RESEARCH ARTICLE

Facies-dependent compositional variation in K-bentonites from lagoonal to littoral environments (Permian-Triassic transition, southwestern China)

Xiaoxue JIN[1], Thomas J. ALGEO[2,3,4], Chen LIU (✉)[1], Hanlie HONG (✉)[1]

1 School of Earth Sciences, China University of Geosciences, Wuhan 430074, China
2 State Key Laboratory of Geomicrobiology and Environmental Changes, China University of Geosciences, Wuhan 430074, China
3 Department of Geosciences, University of Cincinnati, Cincinnati OH 45221-0013, USA
4 State Key Laboratory of Oil and Gas Reservoir Geology and Exploitation, Chengdu University of Technology, Chengdu 610059, China

Abstract The alteration pathways of volcanic ashes depend on the physicochemical conditions of the watermass in which they are deposited. Different conditions in terrestrial, paralic, and marine facies may impart recognizable chemical signatures on altered ash beds (i.e., K-bentonites) that are potentially useful for distinguishing depositional facies in ancient ash-bearing stratigraphic successions. Western Guizhou Province in South China contains widespread Permian-Triassic transition strata from terrestrial lacustrine to shallow-marine shelf facies. In this study, factors influencing the mineralogy and geochemistry of K-bentonites accumulating across a spectrum of freshwater facies in Permian-Triassic transition strata of south-western China were comparatively investigated using mineralogical and geochemical data. Our results show that K-bentonites preserve diagnostic information regarding their depositional environment. The clay mineral assemblages of these K-bentonites are facies-dependent, with dominance of mixed-layer illite/smectite (I/S) clays in freshwater lacustrine facies, kaolinite and I/S in lagoonal facies, mixed-layer kaolinite/smectite (K/S) in mixed marine-terrestrial facies, and smectite and I/S in littoral-neritic facies. The lagoonal Chinahe (CNH) K-bentonites exhibit clay mineral compositions dominated by kaolinite (both highly and poorly crystalline forms) and R1 and R3 I/S clays; the CNH-16 K-bentonite additionally contains minor chlorite. The abundance of kaolinite and absence of smectite in the CNH K-bentonites resulted from strong chemical weathering in an organic acid-rich and oxidizing environment characterized by low porewater pH. The littoral Langdai (LD) K-bentonites contain mainly R1 and R3 mixed-layer illite/smectite (I/S) and smectite, with minor poorly crystalline kaolinite, suggesting a higher pH in seawater-derived pore fluids. The littoral LD K-bentonites and their host sediments have Sr/Ba ratios of 0.34−0.49, consistent with deposition in brackish coastal facies, whereas the higher Sr/Ba ratios of the CNH K-bentonites (0.67−1.07) indicate deposition in a marine to slightly hypersaline lagoonal facies linked to warm, arid climate conditions.

Keywords K-bentonites, mixed-layer illite/smectite (I/S), salinity, porewater pH, sedimentary environment, anatase

1 Introduction

Existing studies of altered volcanic ash beds (i.e., K-bentonites) mostly focus on geochronology and related geochemical characteristics, with little attention given to date to variations in composition linked to the environment of accumulation. However, the secondary mineral assemblage of a K-bentonite depends on the physicochemical conditions of its depositional environment (Erkoyun et al., 2017; Song et al., 2023). Thus, K-bentonites have the potential to preserve diagnostic mineralogical and geochemical signatures that may prove useful for distinguishing depositional facies in ancient ash-bearing stratigraphic successions.

The mineralogical and geochemical signatures acquired by a K-bentonite depend largely on its sedimentary environment and the evolution of pore-fluid chemistry and hydrothermal conditions during diagenesis (Kiipli et al., 2007). For example, alteration of volcanic ash in

Received October 13, 2024; accepted April 8, 2025

E-mails: liuchency@cug.edu.cn (Chen LIU)
honghl8311@aliyun.com (Hanlie HONG)

lacustrine environments produces a combination of mixed-layer illite/smectite (I/S) clays with minor quartz, feldspars, and anatase, with relatively large amounts of MgO and K_2O (Hong et al., 2019), and similar mineral assemblages are generated in swampy and fluvial environments with the addition of minor gypsum and pyrite (Erkoyun et al., 2017). On the other hand, alteration of volcanic ash in marine environments yields different weathering and diagenetic patterns from those of terrestrial environments. K-bentonites in shallow-shelf settings consist mainly of mixed-layer I/S and K-feldspar, whereas those in deep-water settings exhibit more intensive chemical weathering and contain mostly mixed-layer I/S and kaolinite (Kiipli et al., 2007; Hong et al., 2017; Song et al., 2023).

Various trace elements exhibit environmental-specific behaviors that can provide insights into the physicochemical conditions of the depositional system. Redox-sensitive trace metals such as Mo and U have been widely used to reconstruct environmental redox conditions (Algeo and Tribovillard, 2009; Thorpe et al., 2012; Armstrong-Altrin et al., 2015; Wang et al., 2021; Nechaev et al., 2022; Chanu et al., 2023). Other trace elements are salinity dependent, such as B and Sr, and can thus be used to trace salinity variations in the depositional environment (Chen et al., 2020; Wei and Algeo, 2020; Liu et al., 2021; Pillai et al., 2023; Kumar et al., 2024). However, geochemical proxies have only rarely been applied to analysis of the paleoenvironmental conditions of K-bentonite formation (Liu et al., 2021, 2024a; Shen et al., 2021). One recent example is an investigation of coal-bearing Upper Carboniferous K-bentonites in the Datong Basin, which used a range of geochemical proxies to show that kaolinitic claystones formed in freshwater, oxic-anoxic facies whereas I/S claystones formed in brackish, oxic-suboxic facies (Liu et al., 2024a).

Although extensive research has been undertaken on K-bentonites from terrestrial and marine settings (Mitchell et al., 1994; Toulkeridis et al., 1998; Kramer et al., 2001; Heintz et al., 2015; Bozkaya et al., 2016; Liao et al., 2016), K-bentonites in transitional terrestrial-marine (i.e., lagoonal to nearshore littoral) environments have received much less attention to date. Comparisons of K-bentonites from lacustrine and marine settings have shown that their clay mineral compositions have little relationship to type of volcanic source, and that the degree of smectite illitization, ordering in mixed-layer I/S clays, and rare earth element (REE) distributions are mainly dependent upon the type of sedimentary environment (Hong et al., 2017; Gong et al., 2018). For example, K-bentonites in lacustrine settings generally contain mixed-layer I/S clays that are better ordered than those from marine facies.

Western Guizhou Province in south China contains widespread Permian-Triassic transition strata under depositional environments ranging from terrestrial lacustrine to shallow-marine shelf, with coastal mudflats and littoral sands being especially well represented (Song et al., 2019; Wignall et al., 2020). Here, we report the findings of an investigation of mineralogical and geochemical variation in K-bentonites from this region that deposited across an environmental spectrum ranging from lacustrine to paralic to shallow-marine facies. The main goals of our study are 1) to document facies-dependent variation in the mineralogy and geochemistry of K-bentonites in transitional terrestrial-marine environments; 2) to determine whether such differences can be linked to specific physicochemical conditions of the depositional system; and 3) to assess whether the identified mineralogical and geochemical features of K-bentonites can be used diagnostically in paleoenvironmental studies.

2 Sampling and methods

2.1 Sampling

During the Late Permian to Early Triassic periods, the area of western Guizhou to eastern Yunnan provinces in south China was situated in the eastern part of the Paleotethys Ocean, close to the paleo-Equator. In this region, continuous Upper Permian to Lower Triassic stratal successions that accumulated in terrestrial, transitional, and marine facies are well-exposed. The Langdai (LD) section (26°4′49″ N, 105°20′36″ E) is located ~2 km south of Langdai town, along the highway from Langdai to Liangshuichong in the Liuzhi special district, Liupanshui City, western Guizhou Province (Figs. 1 and 2). This succession, which accumulated on the south-western margin of the Yangtze carbonate platform, consists of interbedded green, tan, gray, and

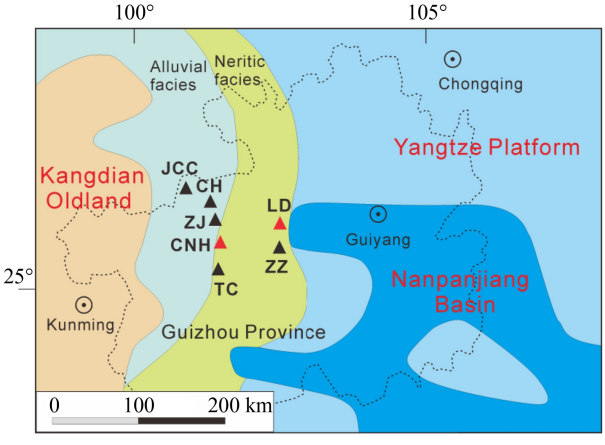

Fig. 1 A generalized map showing the study area and sedimentary facies of study sections of LD (Langdai), CNH (Chinahe), JCC (Jiucaichong), CH (Chahe), ZJ (Zhejue), ZZ (Zhongzhai), and TC (Tucheng). Modified from Yin et al. (2014).

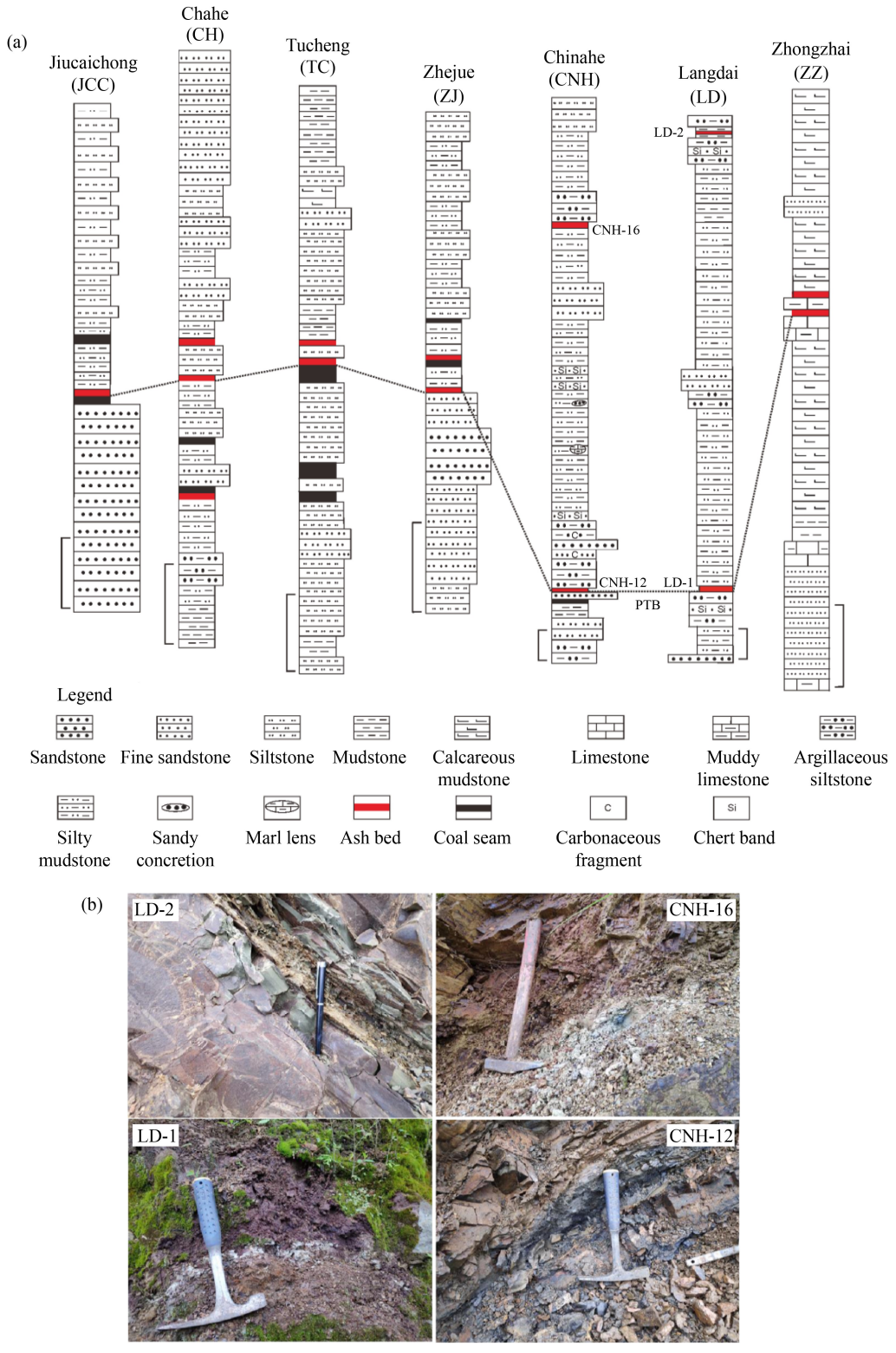

Fig. 2 Distribution of ash beds in Permian-Triassic transition strata of the Langdai (LD) and Chinahe (CNH) sections and other PTB sections of SW China. (a) K-bentonites in the PTB stratigraphic sets along a terrestrial-to-marine transect, south-western Guizhou, China. Modified from Hong et al. (2019), Song et al. (2019), and Shu (2022); each scale bar represents 1 m in length. (b) Close-up images of the Langdai (LD-1, LD-2) and Chinahe (CNH-12, CNH-16) K-bentonites.

brown sandstones, siltstones, mudstones and shales deposited in littoral-neritic facies (Peng et al., 2005). The LD profile comprises the Longtan and Yelang formations. The Longtan Formation is primarily composed of gray-yellow sandstone intercalated with coal seams and gray-green to gray-yellow siltstone, and occasional gray

limestone containing abundant brachiopod fossils, whereas the Yelang Formation is mainly composed of purple-red mudstone with abundant bivalve fossils.

The Chinahe (CNH) section (26°7′12″ N, 104°21′0″ E) is located at Baiyi village alongside the highway near the Chinahe River, Tianba town, Xuanwei City, eastern Yunnan Province, ~330 km west of the Langdai section (Figs. 1 and 2). It consists of the Xuanwei and Kaiyatou formations. The Xuanwei Formation is composed of sandstone, siltstone, and mudstone, interbedded with numerous coal seams and coal lines, and contains abundant Permian gigantopterid plant fossils, indicating a swamp to shallow-lake facies (Bercovici et al., 2015). The lower Kaiyatou Formation is mainly composed of yellowish-green and brownish-yellow siltstone and mudstone with abundant fossils of bivalves, brachiopods, gastropods, leaflets, and plant fossils, whereas the upper Kaiyatou Formation is dominated by fine sandstone and siltstone with rare fossils.

Two K-bentonite beds were observed in each of the study sections. The lower of the two beds is present at the level of the Permian-Triassic boundary (PTB), and the upper one is located 12.95 m above the PTB in the CNH section, representing a time lag of < 0.3 Myr (Wu et al., 2021). Prior to sampling, loose surficial materials were removed using a shovel. Material was then carefully excavated from between layers of the sections using a small trowel, generating ~500-g samples of the fresh K-bentonite and adjacent host rock. For the Langdai section, two samples of K-bentonite (LD-1, LD-2) and two of the adjacent siltstone (LD-1b, LD-2b) were collected; and also for the Chinahe section, two samples of K-bentonite (CNH-12, CNH-16) and two of the adjacent siltstone (CNH-12b, CNH-16b) were collected.

2.2 X-ray diffraction analysis

The fresh K-bentonite samples were dried in an oven at 60°C overnight and were then crushed and ground using an agate mortar and pestle to pass through a 200 mesh (0.74 μm) screen. The powdered sample was treated with 20% hydrogen peroxide to remove organic matter. A small amount of sodium hexametaphosphate was added to the solution, which was then treated with an ultrasonic instrument for 2 min, to fully disperse the clay particles. After settling for ~10 h, the supernatant solution was collected in a centrifuge cup and centrifuged at a speed of 1000 rpm for 4 min to obtain the clay fraction. The bulk K-bentonite samples were prepared by mounting the powders into sample holders using a back-press technique in order to avoid preferential orientation effects, and the oriented clay fractions were prepared by pipetting the purified clay suspension onto glass slides and allowing them to dry at ambient room temperature. Ethylene glycol-saturated treatment of clay fractions was undertaken by reacting a sample aliquot with ethylene glycol vapor in a desiccator at 65°C for 6 h. The oriented clay samples were heated to 400°C for 1 h to distinguish chlorite from expandable clays.

XRD measurements were performed at the State Key Laboratory of Geological Processes and Mineral Resources (GPMR), China University of Geosciences-Wuhan. The X-ray diffractometer was operated at 35 kV and 30 mA with Ni-filtered Cu Kα radiation and the slit system of 1° divergence slit, 1° anti-scatter slit, and 0.3 mm receiving slit. The relative proportions of clay phases and the stacking structures of mixed-layer clay minerals were obtained by fitting the experimental XRD spectra of clay fractions using the NEWMOD II program (Reynolds and Reynolds, 1996).

2.3 Microscopic observations

Scanning electron microscopic (SEM) and high-resolution transmission electron microscopic (HRTEM) observations were undertaken to characterize the morphology of clay minerals and authigenic nanoscale anatase in the K-bentonites. For SEM analysis, an aliquot of powdered whole-rock sample was prepared by gold-coating and then analyzed at the School of Materials Science and Chemistry (SMSC) of China University of Geosciences (Wuhan) using a Hitachi SU8010 High-Resolution Scanning Electron Microscope. HRTEM was employed to observe the morphology of individual authigenic anatase nanoparticles. A small amount of bulk K-bentonite sample was immersed in methanol solution and then ultrasonically dispersed for 10 min. Subsequently, the clay material was collected on a copper grid and dried under an infrared light. HRTEM observation was carried out on a Tecnai G2 20 S-TWIN high-resolution transmission electron microscope equipped with a GENESIS 2000 X-ray energy-dispersive (EDS) at GPMR. The instrument was operated at an accelerating voltage of 160 kV with a beam spot size of 1.5 nm. The point resolution was 0.24 nm and the line resolution was 0.14 nm.

2.4 Geochemical analyses

The major element compositions of the bulk K-bentonites and adjacent siltstones were analyzed using X-ray fluorescence (XRF), which was conducted at GPMR. The loss-on-ignition (LOI) values were measured as the difference in weight of aliquots of dry powdered sample heated to 105°C and 1000°C, and the concentrations of major element oxides were measured through the fused pellet technique. To prepare the fused pellets for XRF analysis, ~1 g of sample along with 5 g of $LiBO_2$ was put in a platinum crucible, with the addition of $Li_2B_4O_7$ as a fluxing agent mixed uniformly in a ratio of 12:22 ($Li_2B_4O_7$:$LiBO_2$). The platinum crucible was heated on a high-temperature furnace at 1100°C for 12 min until

completely melted. Subsequently, the molten mixture was poured into a circular flat glass container and allowed to cool, yielding a fused pellet for XRF analysis. The analysis was carried out using a SHIMADZU XRF-1800 sequential XRF spectrometer, with a rhodium tube and a 2.5 kW generator. For major elements in the bulk samples, detection limits were ~0.01 wt%, and the relative standard deviation was ~1%.

Trace elements and REE analyses were performed at GPMR using inductively coupled plasma mass spectrometry (ICP-MS). To dissolve the bulk sample for ICP-MS measurement, ~0.05 g of dry powdered sample was placed in a clean Teflon digestion bomb. Approximately 1 mL HF and 1 mL HNO_3 were added to the sample, which was then heated to 190°C in an electric oven for 48 h. After completely drying the sample at 120°C, the residue was redissolved in 1 mL of HNO_3 solution and then redried, a process that was repeated three times. Lastly, 1 mL of pure water, 1 mL HNO_3, and internal standards were added to the sample, which was allowed to sit at 190°C for 12 h. Finally, the solution was diluted to 100 mL by adding 2% HNO_3 solution. Elemental measurements were carried out using an Agilent 7500a inductively coupled plasma mass spectrometer (ICP-MS), with relative standard deviations of ~4% for REEs and Y and ~10% for other trace elements.

3 Results

3.1 Mineralogical compositions of the K-bentonites

XRD analysis revealed that both LD K-bentonites have the same mineral assemblage, consisting dominantly clay minerals and minor orthoclase and quartz (Fig. 3(a)). Sample LD-1 contains relatively more quartz and orthoclase but less smectite and kaolinite than Sample LD-2. Both CNH K-bentonites contain mainly clay minerals with minor amounts of quartz and calcite. Sample CNH-12 consists dominantly of kaolinite and mixed-layer I/S with minor quartz, whereas Sample CNH-16 contains mixed-layer I/S, kaolinite, and chlorite, as well as more abundant quartz and calcite. The most significant difference in the mineralogical assemblages of the K-bentonites between the two sections is the presence of smectite in the LD K-bentonites versus its absence in the CNH K-bentonites.

In the XRD patterns of clay fractions of the LD K-bentonites, the 14.5−15.0 Å peak in the air-dried samples expanded to 17 Å after ethylene glycol saturation, and collapsed to 10 Å after heating to 400°C, indicating the presence of smectite (Figs. 3(b) and 3(c)). The strong peak at ~10.7 Å decomposed into two peaks near ~9.5 Å and ~12.0 Å after glycolated treatment, indicating the presence of an ordered mixed-layer I/S clay phase. In the XRD patterns of clay fractions of the CNH K-bentonites, the ~11.6 Å peak of mixed-layer I/S clays decomposed into two peaks near ~9.7 Å and ~12.7 Å after saturation with ethylene glycol. The 14 Å and 3.52 Å peaks together with the 7.15 Å and 3.58 Å peaks in the air-dried sample did not change when treated with ethylene glycol saturation and heating to 400°C, confirming the occurrence of chlorite and kaolinite in Sample CNH-16.

Fitting of the XRD patterns of glycolated clay fractions showed that all K-bentonites from the study sections contain mixed-layer I/S clay components having both R1 and R3 stacking structures (Fig. 4). The relative abundances of clay species in Sample LD-1 are 16.3% smectite, 15.9% kaolinite, and 67.9% mixed-layer I/S clays (24.1% R1 and 43.8% R3), and in Sample LD-2 are 46.5% smectite, 10.5% kaolinite, and 43.1% I/S clays (38.1% R1 and 5.0% R3). Kaolinite in both the LD K-bentonites exhibits generally poor crystallinity. Clay minerals in the CNH K-bentonites consist mainly of two types of kaolinite (one highly crystalline and the other poorly crystalline) and I/S clays: Sample CNH-12 contains 54.4% highly crystalline kaolinite, 17.8% poorly crystalline kaolinite, and 27.9% I/S (11.8% R1 and 16.1% R3), and Sample CNH-16 contains 14.4% highly crystalline kaolinite, 9.1% poorly crystalline kaolinite, 16.4% chlorite, and 60.2% I/S (28.9% R1 and 31.3% R3).

3.2 Morphology of clay minerals and authigenic anatase in the K-bentonites

K-bentonites exhibit a generally loose texture under SEM observation. However, the micromorphology of clay grains exhibits marked differences between the samples. Clay flakes usually occur in clay aggregates in the LD K-bentonites, in which smectite aggregates are enclosed by volcanic ash particles or occupy their interstitial spaces. Smectite flakes in the interstitial space among ash particles display an interwoven structure and their aggregates show a honeycombed polygonal pattern (Fig. 5(a)). Volcanic ash particles with irregular outlines were replaced by newly formed smectite flakes (Fig. 5(b)). In general, clay flakes in the CNH samples exhibit an uneven basal (001) plane with typically curled edges and a wavy outline. Kaolinite in poorly developed pseudo-hexagonal plates with a relatively smooth or flat basal (001) plane occurs closely associated with wavy I/S plates (Fig. 5(c)). Mixed-layer I/S clays display angular and irregular outlines, and their aggregates exhibit a swirly texture with face-to-face arrangement of clay grains (Fig. 5(d)).

HRTEM observations showed that, although parts of the anatase grains have anhedral morphology, most of authigenic anatase crystals exhibit distinct euhedral morphology with a size of 0.1 to 1.0 μm (Figs. 5(e)−5(h)). Anatase crystals in Sample LD-1 are dominantly tetragonal bipyramidal in shape with generally straight

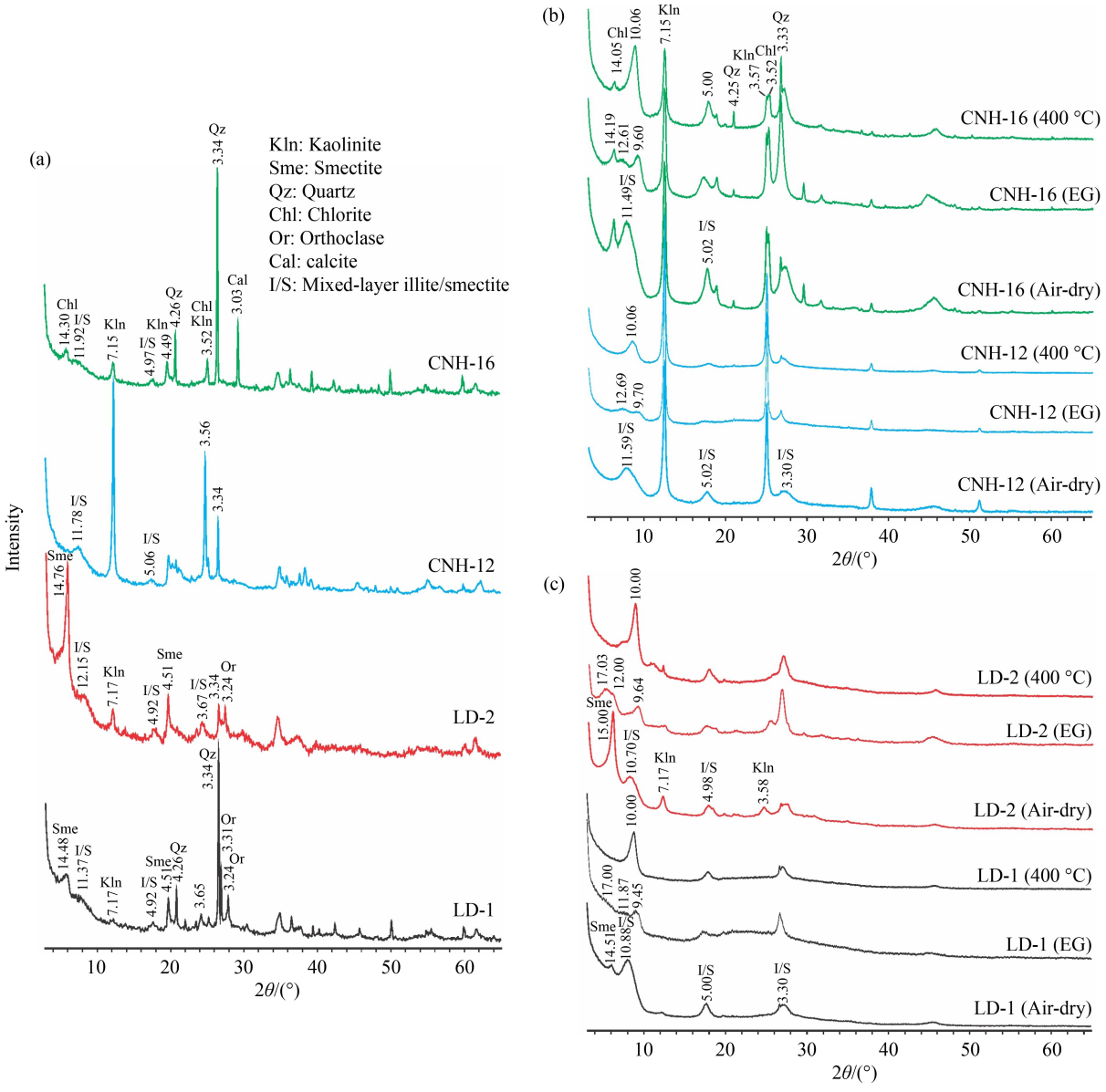

Fig. 3 XRD patterns of the LD and CNH K-bentonites showing their mineral compositions. (a) Bulk K-bentonites; (b–c) clay fractions of air-dried (AD), ethylene-glycolated (EG) saturation, and heating to 400°C.

margins, whereas those in Sample LD-2 are mostly anatase nanoparticles with euhedral tetragonal and short prismatic morphologies. Anatase shows a distinctively irregular morphology with no euhedral shapes in Sample CNH-12, where it occurs as spongy aggregates. Anatase in Sample CNH-16 displays tetragonal bipyramidal morphologies (similar to those in Sample LD-1), although some crystals exhibit a truncated shape.

3.3 Major geochemical composition of K-bentonites

The K-bentonite samples exhibit quite different geochemical compositions between the two study sections, with only minor components such as K_2O, P_2O_5, and LOI having similar values (Table 1). Samples from the LD section have relatively lower LOI values (6.64% to 7.52%) relative to those from the CNH section (10.99% to 11.32%), consistent with differences in their clay mineral compositions (i.e., dominantly smectite and mixed-layer I/S at LD, and mainly kaolinite and mixed-layer I/S at CNH).

Geochemical differences are also apparent between the K-bentonites of each individual section. Relative to Sample LD-2, Sample LD-1 contains substantially more SiO_2 (53.83% vs. 47.14%), Al_2O_3 (21.64% vs. 18.58%), Na_2O (0.62% vs. 0.21%), and K_2O (4.95% vs. 4.32%), and less TFe_2O_3 (5.74% vs. 13.02%), MgO (3.27% vs. 5.43%), and CaO (1.37% vs. 2.14%). They have similar contents of TiO_2 (1.18% vs. 1.20%), MnO (0.12% vs. 0.14%), and P_2O_5 (0.23% vs. 0.21%). Relative to Sample

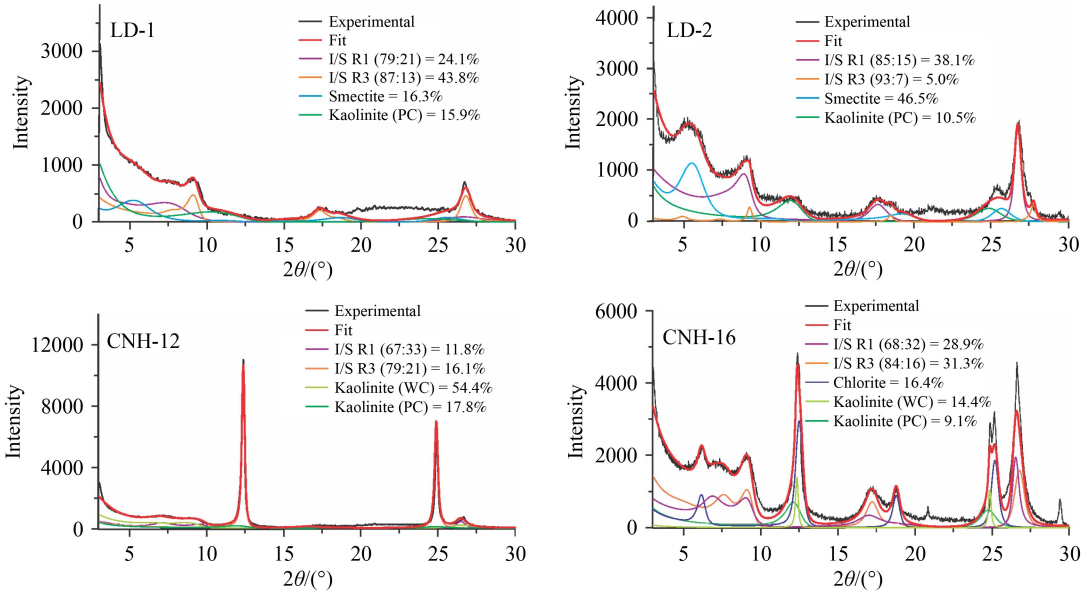

Fig. 4 XRD fitting patterns of glycolated clay fractions showing the stacking structures of mixed-layer clays and the relative contents of clay species in the LD and CNH K-bentonites.

CNH-16, Sample CNH-12 contains notably more Al_2O_3 (33.00% vs. 16.25%) but less TiO_2 (0.99% vs. 2.07%), TFe_2O_3 (3.01% vs. 7.01%), MnO (0.01% vs. 0.25%), MgO (0.48% vs. 2.36%), CaO (0.56% vs. 9.03%), K_2O (2.39% vs. 3.02%), and P_2O_5 (0.20% vs. 0.29%). They have similar contents of SiO_2 (47.99% vs. 47.20%) and Na_2O (0.03% vs. 0.04%).

3.4 Trace-element and REE concentrations

Three of the K-bentonite samples (LD-1, LD-2, and CNH-16) exhibit similar chondrite-normalized REE trace element and primitive-mantle-normalized distributions (Fig. 6(a)). They are characterized by a right-tending REE distribution pattern with no Eu anomaly. In contrast, Sample CNH-12 shows light rare earth element (LREE) enrichment and relatively flat heavy rare earth element (HREE) profiles, with a slightly negative Eu anomaly.

The ΣREE values of samples LD-1 and LD-2 are 667 ppm (parts per million) and 290 ppm, and those of CNH-12 and CNH-16 are 187 ppm and 343 ppm, respectively (Table 2). The LD K-bentonite samples have ΣLREE and ΣHREE values of 611−269 ppm and 55.8−20.4 ppm, and the CNH K-bentonite samples ΣLREE values of 149–310 ppm and ΣHREE values of 37.5–32.9 ppm, respectively. However, the ΣLREE/ΣHREE ratios (10.9−13.2) of the LD K-bentonite samples are relatively higher than those of 4.0−9.4 for the CNH K-bentonite samples. The primitive-mantle-normalized distribution patterns of samples LD-1, LD-2, and CNH-16 show pronounced negative Ba, Nb, and Sr anomalies and evident positive Th, La, Pr, Nd, and Zr anomalies, whereas Sample CNH-12 exhibits generally more pronounced negative Ba, Ce, Sr, and Eu anomalies but positive Th, U, Pb, Zr, and Hf anomalies (Fig. 6(b); Table 2).

4 Discussion

4.1 Sedimentary environmental dependence of clay mineralogy in K-bentonites

The mineral composition of a K-bentonite depends largely on its source material, sedimentary environment, and depositional and diagenetic histories (Kiipli et al., 2007; Ver Straeten, 2008; Bozkaya et al., 2016; Osacký et al., 2023). Previous investigations of phenocrysts, accessory minerals, and trace elements of the K-bentonites in south China PTB sections have shown that they were sourced from intermediate-felsic magmas generated along the South China-Indochina and/or South China–Panthalassic plate margins (Stampfli and Borel, 2002; Isozaki et al., 2007; Hong et al., 2019). K-bentonites form through devitrification of volcanic ash, which can take place during early or late diagenesis (Fortey et al., 1996). During the Permian-Triassic transition, volcanic ashes deposited in the terrestrial-marine environments of the South China Craton experienced a unified tectonic history and formed under a limited range of burial conditions (He et al., 2014). Therefore, minor variations in the depositional and diagenetic histories of PTB volcanic ashes in South China were probably not the main factors influencing their alteration patterns. Rather, the chemistry of the local depositional environment (especially porewater composition and pH) was generally the key influence (Kiipli et al., 2007).

The presence of authigenic clay minerals and non-clay minerals of orthoclase, quartz, and calcite in the K-bentonites of the two study sections suggests formation from alteration of primary volcanic ash deposits. Differences in the mineral assemblages of the K-

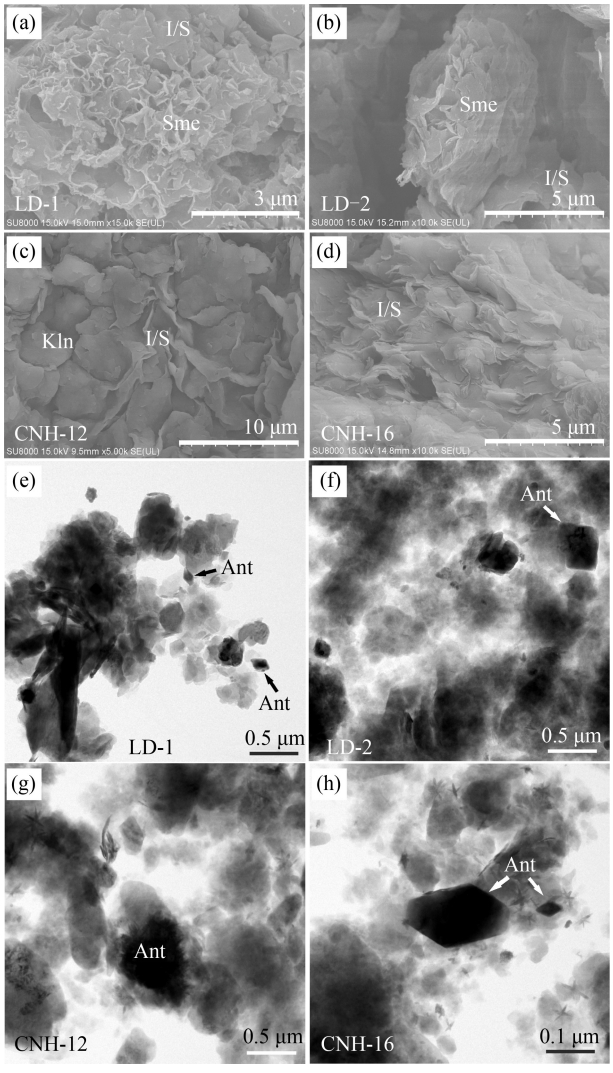

Fig. 5 Microscopic observations of morphologies of clay minerals (A-D, SEM) and authigenic anatase crystals (E-H, HRTEM) in the LD and CNH K-bentonites: (a), (b) smectite showing typical honeycombed polygonal (LD-1) and wave-shaped (LD-2) aggregates in the LD K-bentonites; (c) poorly developed pseudo-hexagonal kaolinite associated with wave-shaped I/S plates in CNH-12; (d) mixed-layer I/S aggregates having a swirly texture with face-to-face arrangement of clay flakes in CNH-16; (e) anatase with tetragonal bipyramidal shapes in LD-1; (f) anatase with tetragonal and short prism morphologies in LD-2; (g) anatase in sponge-like aggregates in CNH-12; and (h) anatase in truncated tetragonal bipyramidal crystals in CNH-16.

bentonites (i.e., greater smectite in LD, greater kaolinite in CNH and, for CNH-16, greater chlorite content; Fig. 3) provide insights into the depositional and diagenetic histories of these units. They represent a range of freshwater lacustrine, lagoonal, mixed marine-terrestrial, and littoral-neritic facies that are dominated, respectively, by mixed-layer I/S clays, kaolinite and I/S, kaolinite and K/S, and smectite and I/S (Hong et al., 2019).

The alteration of volcanic ash depends mainly on conditions of solution pH, organic matter, porewater composition, and microbial activity, which are largely environmentally controlled (Hints et al., 2008; Huff, 2016; Song et al., 2023). During the weathering and alteration of ash in seawater, dissolution of K is accompanied by incorporation of Mg and Ca from seawater during devitrification of volcanic glass and neoformation of smectite (Püspöki et al., 2008). Subsequently, neoformed smectite will further convert to mixed-layer I/S minerals, in which the illite-layer content and structural ordering are largely dependent on burial temperature (Šucha et al., 1993) and porewater chemistry (Clauer et al., 2022). The LD K-bentonites contain highly ordered R1 and R3 mixed-layer I/S clays and smectite, with minor poorly crystalline kaolinite (Fig. 4). The co-existence of smectite and highly ordered R1 and R3 I/S clays in the K-bentonites indicate transformation of smectite to illite as burial temperature increases. Porewater pH is also considered as one of the major factors influencing illitization of smectite. In shallow-water settings, intense bioproductivity favors the consumption of CO_2 and results in an increase in seawater pH. This process facilitates the uptake of cations from seawater and, thus, the formation of feldspars rather than clay minerals, inhibiting illitization of smectite (Kiipli et al., 2007; Lei et al., 2022). In addition, high-energy shallow-water settings often experience significant loss of porewater cations, which limits the amount of K available for illitization of smectite during burial diagenesis (Caballero et al., 1992; Mills et al., 2023). The co-existence of smectite and orthoclase in the LD K-bentonites attests to the limited assimilation of K by ash-derived clays linked to preferential formation of orthoclase in the burial environment.

The two CNH K-bentonites contain mainly kaolinite and ordered R1 and R3 mixed-layer I/S clays, while the upper one (CNH-16) also contains minor chlorite (Fig. 4). Kaolinite is the most common soil-derived clay mineral formed through weathering and alteration of igneous rocks under warm/humid tropical to subtropical climate conditions (Núñez and Recio, 2007). During diagenetic alteration of volcanogenic sediments, intense leaching in an acidic environment and lack of potassium results in formation of kaolinite (Hints et al., 2008; Liu et al., 2021). Therefore, the occurrence of large amounts of kaolinite in the CNH K-bentonites may indicate that acidic conditions prevailed during the alteration process. Although the LD K-bentonites contain minor amounts of poorly crystalline kaolinite, the CNH K-bentonites consist dominantly of highly crystalline kaolinite with minor poorly crystalline kaolinite (Fig. 4). The poorly crystalline kaolinite was probably derived from post-depositional alteration of ash, as formation of this type of kaolinite is usually promoted by seasonal wetting and drying cycles during ash deposition (Püspöki et al., 2008), which is consistent with the generally warm and humid paleoclimate of South China during the Permian-Triassic transition (Yin et al., 2014). During diagenesis,

Table 1 Major chemical compositions of K-bentonite and adjacent siltstone samples in this and other studies (all values are wt%)

Section	SiO_2	TiO_2	Al_2O_3	Fe_2O_3	MnO	MgO	CaO	Na_2O	K_2O	P_2O_5	LOI	SUM	Section	Note
JCC-1	51.38	0.52	27.14	2.54	0.10	2.34	0.13	0.00	6.49	0.04	9.69	100.37	Jiucaichong	Hong et al. (2019)
CH-2	48.74	0.71	26.43	7.54	0.24	1.31	0.27	0.02	5.30	0.11	9.17	99.84	Chahe	Gong et al. (2018)
CH-1	57.47	2.62	21.61	3.73	0.00	0.79	0.31	0.00	4.45	0.05	9.42	100.45	Chahe	Gong et al. (2018)
TC-2	51.18	4.42	26.78	3.87	0.01	0.40	0.07	0.00	0.82	0.16	12.83	100.54	Tucheng	Hong et al. (2017)
TC-1	49.58	4.75	28.85	3.42	0.01	0.43	0.09	0.00	0.84	0.15	12.45	100.57	Tucheng	Hong et al. (2017)
ZJ-2	46.90	6.47	30.50	2.11	0.02	0.43	0.17	0.13	1.97	0.06	11.67	100.43	Zhejue	Hong et al. (2017)
ZJ-1	47.78	6.34	29.53	2.28	0.01	0.53	0.19	0.07	1.58	0.19	11.90	100.40	Zhejue	Hong et al. (2017)
CNH-16b	49.14	2.36	13.67	12.38	0.28	3.05	6.20	0.18	2.00	0.33	8.79	98.39	Chinahe	This study
CNH-16	47.20	2.07	16.25	7.01	0.25	2.36	9.03	0.04	3.02	0.29	11.32	98.84	Chinahe	This study
CNH-12b	45.10	4.65	18.02	16.86	0.72	1.39	1.59	0.03	1.53	0.57	9.82	100.26	Chinahe	This study
CNH-12	47.99	0.99	33.00	3.01	0.01	0.48	0.56	0.03	2.39	0.20	10.99	99.64	Chinahe	This study
LD-2b	51.57	2.30	16.28	10.67	0.13	4.82	2.69	0.89	4.06	0.43	5.65	99.48	Langdai	This study
LD-2	47.14	1.20	18.58	13.02	0.14	5.43	2.14	0.21	4.32	0.21	7.52	99.92	Langdai	This study
LD-1b	58.47	2.54	14.98	9.28	0.48	1.77	1.41	2.87	2.60	0.52	4.35	99.26	Langdai	This study
LD-1	53.83	1.18	21.64	5.74	0.12	3.27	1.37	0.62	4.95	0.23	6.64	99.59	Langdai	This study
ZZ-2	52.14	0.94	20.30	5.19	0.28	3.23	1.33	0.04	4.14	0.12	12.75	100.46	Zhongzhai	Hong et al. (2017)
ZZ-1	54.79	0.56	20.34	3.30	0.45	3.22	1.85	0.07	3.76	0.13	12.03	100.50	Zhongzhai	Hong et al. (2017)

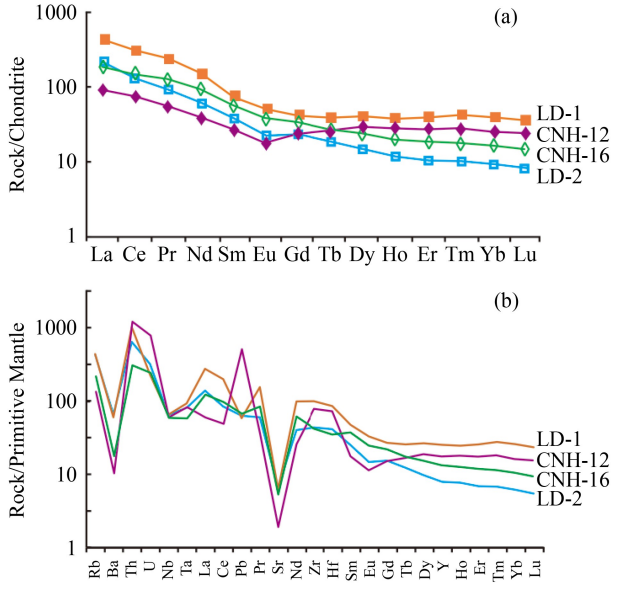

Fig. 6 (a) Chondrite-normalized REE distributions, and (b) primitive-mantle-normalized trace element distributions of the LD and CNH K-bentonites.

the low-energy lagoonal setting of the CNH K-bentonites facilitated retention of porewater cations (including K) and, thus, promoted illitization of smectite (Caballero et al., 1992; Somelar et al., 2010; Clauer et al., 2022), resulting in the lower smectite contents of these K-bentonites (Fig. 4).

Chlorite is a common mineral in greenschist-grade metamorphic rocks that can also form in porewaters during sediment diagenesis. Chlorite is often found in sedimentary rocks and may survive repeated erosional cycles, thus being a common detrital clay mineral under conditions of dominantly physical weathering in cold and dry climates (Alizai et al., 2012). The presence of mainly I/S clays and minor chlorite in the K-bentonite suggests that the deposition of CNH-16 volcanic ash was associated with detrital chlorite input of terrestrial weathering origin due to clay segregation in the marine environment. Chlorite tends to be deposited rapidly in marine environments after riverine delivery, resulting in higher concentrations in nearshore areas (Chamley, 1989). The occurrence of minor amounts of calcite in Sample CNH-16 probably indicates a nearshore shallow-water environment (Figs. 3 and 4), in which detrital sediment may form condensed deposits during sea-level transgression (Püspöki et al., 2008).

4.2 Geochemical proxies linked to environmental changes across the study area

Sr/Ba ratios can be used to evaluate depositional watermass salinity, subject to certain constraints. For fine-grained siliciclastic sediments, Sr/Ba ratios of < 0.2, 0.2−0.5, and > 0.5 are indicative of freshwater (< 1 psu), brackish (1−30 psu), and marine salinities (30−40 psu), respectively (Wei and Algeo, 2020; n.b., psu = practical salinity unit). The relationship of salinity to sediment Sr/Ba ratios exists because the Sr concentration of a watermass scales linearly with its salinity, and aqueous Sr is readily adsorbed by clay minerals in the sediment.

The study samples yield Sr/Ba-based salinity estimates

Table 2 Concentrations of trace elements and REEs of K-bentonite and adjacent siltstone samples in this and other studies (all values are 10^{-6})

Section	Li	Be	Sc	V	Cr	Co	Ni	Cu	Zn	Ga	Rb	Sr	Y	Zr	Nb	Sn	Cs	Ba	La	Ce	Pr	Nd	Sm
JCC-1	37.2	1.83	7.73	18.4	4.92	6.02	19.1	16.1	60.5	17.0	67.5	318	54.2	340	15.3	6.40	8.21	37.4	74.5	131	15.7	58.8	12.1
CH-2	1.62	5.08	32.6	265	214	5.25	28.2	132	27.2	28.8	105	35.5	132	295	31.9	3.00	3.01	108	222	341	84.4	361	76.7
CH-1	3.14	3.36	15.8	33.2	13.0	14.7	25.6	128	45.8	34.9	226	22.6	59.0	554	31.8	10.7	11.8	163	31.3	86.4	12.4	53.2	12.2
TC-2	19.5	3.27	27.1	293	83.4	7.96	58.9	126	45.8	34.8	33.2	272	79.8	555	57.8	5.11	1.97	403	105	213	30.7	130	26.4
TC-1	20.4	2.68	26.2	272	75.7	9.08	49.1	123	51.3	34.2	37.0	180	74.2	535	53.3	4.58	1.83	292	101	194	28.5	116	22.4
ZJ-2	34.6	2.37	5.61	41.7	15.6	6.03	28.8	7.07	19.4	26.1	9.55	12.3	8.83	343	16.6	10.0	0.42	36.7	11.6	20.3	2.26	8.20	1.51
ZJ-1	13.5	2.90	35.6	385	272	8.05	77.4	144	77.3	34.1	51.3	96.7	68.8	664	53.1	4.38	2.10	158	112	222	26.6	100	15.6
CNH-16b	14.2	2.76	21.5	197	93.3	44.6	63.3	161	105	22.8	82.2	71.3	37.3	308	34.8	4.03	2.25	102	53.8	116	14.0	50.5	10.4
CNH-16	13.8	3.58	19.9	168	74.3	21.8	40.7	95.6	82.8	24.7	119	101	47.4	358	33.7	4.80	7.16	94.5	68.0	140	17.6	67.0	13.3
CNH-12b	40.3	3.82	37.9	384	159	78.9	116	253	235	35.3	53.3	88.2	57.2	491	66.0	4.71	1.91	234	81.0	182	20.7	82.4	16.1
CNH-12	65.3	5.18	25.4	68.9	17.8	9.92	18.6	39.8	81.5	32.6	73.9	36.9	62.2	661	34.4	12.0	7.85	55.4	33.6	71.8	7.67	28.4	6.39
LD-2b	38.7	5.21	20.5	194	67.0	30.0	52.2	114	85.1	28.5	186	266	46.1	387	46.8	5.43	5.35	541	62.8	125	15.9	62.0	13.1
LD-2	45.7	4.74	15.8	210	42.0	30.8	46.5	54.2	102	30.6	245	118	27.1	371	37.1	9.87	13.6	342	78.5	124	12.6	43.8	8.88
LD-1b	28.4	2.52	20.6	207	113	34.1	62.5	95.0	136	23.1	98.4	337	43.3	319	41.4	3.06	3.27	545	54.3	116	13.1	53.3	11.1
LD-1	39.1	8.97	31.3	141	85.3	17.3	29.6	27.3	64.6	35.4	248	112	87.4	847	37.4	11.5	16.5	312	156	292	32.8	108	16.8
ZZ-2	20.7	2.22	26.1	90.0	17.3	13.2	18.5	24.1	88.8	29.1	176	35.4	40.5	430	20.9	5.87	5.44	143	32.2	147	8.52	31.7	8.06
ZZ-1	12.6	4.24	14.9	44.3	26.0	7.06	21.0	19.9	69.0	25.3	138	179	74.0	411	18.5	6.32	7.19	137	73.7	126	17.4	64.6	13.3

Section	Eu	Gd	Tb	Dy	Ho	Er	Tm	Yb	Lu	Hf	Ta	Tl	Pb	Th	U	∑REE	∑LREE	∑HREE	∑LREE/∑HREE	Note
JCC-1	1.56	11.2	1.78	10.6	2.00	5.44	0.77	4.61	0.65	10.2	1.69	0.27	72.2	33.9	6.52	340.97	293.80	47.17	6.23	Hong et al. (2019)
CH-2	19.9	63.3	7.85	34.9	5.32	11.6	1.42	7.52	1.04	7.93	2.01	0.31	6.28	11.2	3.10	805	1237.95	132.95	8.31	Gong et al. (2018)
CH-1	3.88	11.7	1.90	11.0	2.11	5.74	0.86	5.67	0.81	17.0	2.97	0.54	2.58	69.9	10.9	239.17	199.38	39.79	5.02	Gong et al. (2018)
TC-2	6.74	22.2	3.14	16.8	3.00	7.84	1.10	6.56	0.94	14.4	2.87	0.21	29.0	16.9	4.80	573.32	511.70	61.62	8.30	Hong et al. (2017)
TC-1	5.80	18.6	2.67	14.2	2.66	6.92	0.94	5.83	0.85	14.0	3.01	0.13	16.8	16.2	4.69	520.96	468.27	52.68	8.89	Hong et al. (2017)
ZJ-2	0.32	1.31	0.25	1.74	0.35	1.09	0.18	1.27	0.19	12.5	2.20	0.04	4.16	38.9	5.21	63.04	44.16	18.89	2.34	Hong et al. (2017)
ZJ-1	3.26	12.5	2.18	13.7	2.62	7.24	1.02	6.25	0.87	17.1	3.54	0.16	19.6	20.0	5.13	543.32	479.82	63.50	7.56	Hong et al. (2017)
CNH-16b	2.58	8.90	1.32	7.75	1.50	3.95	0.53	3.47	0.53	8.29	2.23	0.26	9.53	11.7	2.45	275.5	247.5	28.0	8.85	This study
CNH-16	3.36	10.4	1.58	9.19	1.69	4.68	0.65	4.12	0.57	9.73	2.37	0.30	8.21	19.5	4.34	342.6	309.7	32.9	9.40	This study
CNH-12b	3.63	13.5	2.05	11.6	2.18	5.61	0.73	4.84	0.70	13.2	4.12	0.17	14.4	14.8	3.49	427.3	386.2	41.1	9.39	This study
CNH-12	1.57	7.28	1.52	11.3	2.40	6.81	1.02	6.30	0.93	19.9	3.35	0.17	60.2	74.9	13.7	186.9	149.4	37.5	3.98	This study
LD-2b	3.03	10.9	1.71	9.06	1.68	4.56	0.65	4.11	0.57	10.3	3.13	0.34	7.07	18.5	4.24	315.4	282.1	33.2	8.49	This study
LD-2	1.95	7.14	1.08	5.64	1.00	2.60	0.37	2.31	0.31	11.4	3.31	0.37	7.71	42.4	5.94	289.7	269.3	20.5	13.17	This study
LD-1b	2.55	9.19	1.30	7.84	1.44	3.85	0.53	3.17	0.48	8.40	2.52	0.35	11.2	10.8	3.57	277.9	250.1	27.8	9.00	This study
LD-1	4.38	12.6	2.26	15.4	3.20	9.73	1.52	9.73	1.36	23.5	3.81	0.25	7.17	67.7	4.26	666.8	611.0	55.8	10.95	This study
ZZ-2	1.71	7.44	1.33	7.66	1.52	4.33	0.63	3.70	0.54	11.7	1.74	0.41	43.8	28.4	4.45	256.06	228.91	27.15	8.43	Hong et al. (2017)
ZZ-1	2.83	12.8	2.17	13.0	2.63	7.78	1.14	6.65	0.97	12.0	1.58	0.28	42.6	31.2	4.20	345.39	298.45	47.15	6.33	Hong et al. (2017)

that are consistent with their inferred depositional settings (Table 3). The lacustrine JCC and CH K-bentonites exhibit low Sr/Ba ratios (0.09−0.14) indicative of freshwater conditions. The K-bentonites that accumulated in nearshore littoral environments such as those in the LD, ZZ, and ZJ sections have Sr/Ba ratios mostly in the range of 0.25−0.49, consistent with a brackish depositional environment (cf. Liu et al., 2021). These sections may represent a low-energy, mud-dominated coastal "lagoonal" facies belt (Bercovici et al., 2015). The K-bentonites from mixed marine-terrestrial and paludal environments show higher Sr/Ba ratios (0.61−0.67), suggestive of fully marine salinity conditions. The CNH K-bentonites and adjacent sediments yield even higher Sr/Ba ratios (0.67−1.07) (Table 3), perhaps indicative of transient climate aridification and watermass hypersalinity (Wignall et al., 2020).

Several factors in addition to salinity may have

Table 3 Calculated geochemical indices of K-bentonites and host sediments in terrestrial to littoral environment in in western Guizhou Province

Section	CIA[a)]	MgO/K_2O	MgO/Al_2O_3	TiO_2/Al_2O_3	Sr/Ba	Y/Ho	U/Th	U_{EF} [b)]	Sedimentary facies	Section	Lithology	Note
JCC-1	79.4	0.843	0.218	0.024	0.09	27.10	0.19	1.3	Lacustrine	Jiucaichong	K-bentonite	Hong et al. (2019)
CH-2	82.3	0.578	0.125	0.034	0.33	24.81	0.28	0.6	Lacustrine	Chahe	K-bentonite	Gong et al. (2018)
CH-1	82.1	0.415	0.093	0.155	0.14	27.96	0.16	2.7	Lacustrine	Chahe	K-bentonite	Gong et al. (2018)
TC-2	96.8	1.140	0.038	0.211	0.67	26.60	0.28	1.0	Marine-terrestrial transitional	Tucheng	K-bentonite	Hong et al. (2017)
TC-1	96.9	1.196	0.038	0.210	0.62	27.89	0.29	0.9	Marine-terrestrial transitional	Tucheng	K-bentonite	Hong et al. (2017)
ZJ-2	93.8	0.510	0.036	0.271	0.34	25.23	0.13	0.9	Paludal	Zhejue	K-bentonite	Hong et al. (2017)
ZJ-1	92.2	0.784	0.045	0.274	0.61	26.26	0.26	0.9	Paludal	Zhejue	K-bentonite	Hong et al. (2017)
CNH-16b	83.2	3.564	0.565	0.221	0.70	24.87	0.21	1.0	Lagoonal	Chinahe	siltstone	This study
CNH-16	82.7	1.823	0.367	0.163	1.07	28.05	0.22	1.4	Lagoonal	Chinahe	K-bentonite	This study
CNH-12b	91.2	2.121	0.195	0.330	0.38	26.24	0.24	1.1	Lagoonal	Chinahe	siltstone	This study
CNH-12	92.4	0.473	0.037	0.038	0.67	25.92	0.18	2.3	Lagoon	Chinahe	K-bentonite	This study
LD-2b	69.0	2.772	0.748	0.180	0.49	27.44	0.23	1.4	Littoral	Langdai	siltstone	This study
LD-2	77.5	2.935	0.740	0.083	0.34	27.10	0.14	1.7	Littoral	Langdai	K-bentonite	This study
LD-1b	65.3	1.586	0.299	0.217	0.36	30.07	0.33	1.3	Littoral	Langdai	siltstone	This study
LD-1	74.5	1.540	0.383	0.070	0.36	27.31	0.06	1.1	Littoral	Langdai	K-bentonite	This study
ZZ-2	81.5	1.823	0.403	0.059	0.25	26.64	0.16	1.2	Littoral	Zhongzhai	K-bentonite	Hong et al. (2017)
ZZ-1	82.5	2.001	0.401	0.035	1.31	28.14	0.13	1.1	Littoral	Zhongzhai	K-bentonite	Hong et al. (2017)

Notes: a) CIA = Al_2O_3 / (Al_2O_3 + CaO* + K_2O + Na_2O) × 100%, CaO* referring to the Ca in silicates (Nesbitt and Young, 1982; Algeo et al., 2025); b) U_{EF}: enrichment factor of U calculated as the ratio of the measured concentration of a particular element in a sample to its concentration in average upper continental crust (McLennan, 2001).

influenced sediment Sr/Ba ratios. First, the presence of carbonate-sourced Sr can lead to increased Sr/Ba ratios because carbonate minerals such as calcite and aragonite contain large amounts of structural Sr in their lattices (Wei and Algeo, 2020; Wang et al., 2021). The high Sr/Ba ratios of the CNH-16 (1.07) and ZZ-1 K-bentonites (1.31) may be due to the presence of calcite in these samples (Fig. 3(a); Hong et al., 2019). Second, chemical weathering can be an important influence because it usually leads to enhanced release of Sr from silicates (Nesbitt and Markovics, 1997). The CNH and TC K-bentonites, which exhibit high Sr/Ba ratios, also experienced intense chemical weathering, as indicated by the chemical index of alteration (CIA) (Nesbitt and Young, 1982; Algeo et al., 2025) and mineral compositions consisting mainly of kaolinitic clays (Table 3).

The retention of aqueous Sr and Ba by neoformed clay minerals in K-bentonites also depends on redox conditions (Renock et al., 2016). Ba mobility is reduced in oxic environments, in which it tends to form highly insoluble barite ($BaSO_4$) given availability of sulfate, and greater in anoxic environments in which sulfate concentrations decrease as a result of intense microbial sulfate reduction (Kasten and Barker-Jorgensen, 2000; Wang et al., 2021). This may account for the difference in Sr/Ba ratios between the CNH-12 K-bentonite (0.66) and CNH-16 K-bentonite (1.07). The CNH-12 K-bentonite was deposited in a mildly reducing system, as shown by its enrichment in U (U_{EF} = 2.3) relative to other CNH samples (U_{EF} = 1.0−1.4; Table 3), which may have been due to the proximity of a coal seam, leading to decay of organic matter and enhanced acidity and reduced Eh in the burial environment (Liu et al., 2021). These conditions favored the retention of Ba in the CNH-12 K-bentonite and, thus, a lower Sr/Ba ratio relative to the CNH-16 K-bentonite (Wang et al., 2021).

The elements Y and Ho have an identical charge and similar ionic radii, making the Y/Ho proxy useful for tracking weathering, transport, and depositional processes (Bau et al., 1996). Intermediate igneous rocks and shales have Y/Ho ratios of 25−30 and modern seawater has a value of 44−74 (McLennan, 1989; Bau et al., 1996). In this study, both K-bentonites and adjacent mudstones exhibit Y/Ho ratios within the narrow range of 24.8 to 30.1 (Table 3), compatible with those of typical crustal materials. These values suggest that fractionation of Y and Ho (and other REEs) was negligible during alteration of the PTB K-bentonites in environments ranging from lacustrine to littoral marine, and that the REE fraction of the sediment was derived from crustal sources rather than from seawater (Bau et al., 1996).

Th and U are both relatively immobile during weathering, but strongly oxidizing condition facilitates solubility of U and, thus, decreases in the U/Th ratio, as U^{4+} is insoluble and U^{6+} is soluble in highly oxic

environments (Sheldon and Tabor, 2009). Sediment U/Th ratios of < 1.25 and > 1.25 indicate oxic and anoxic conditions, respectively (Jones and Manning, 1994). Samples from the lacustrine environment and nearshore littoral sections display generally lower U/Th ratios of 0.06−0.33, suggesting oxic conditions during deposition (Table 3). However, samples from nearshore littoral sections in the upper section exhibit relatively higher U/Th values than those of the lower section, implying a decrease in redox state. Variations of U/Th from 0.06 to 0.14 and from 0.18 to 0.22 in the LD and CNH sections probably reflect redox variation between a high-energy, shallow littoral environment at LD and a lower-energy, slightly deeper lagoonal environment at CNH, consistent with variations in authigenic anatase morphology in the K-bentonites (Hong et al., 2020, 2022; Liu-C et al., 2024b).

4.3 Implications for depositional and diagenetic conditions

The K content of a K-bentonite is largely dependent on its parent volcanic glass as well as the salinity of the groundwater in the depositional system, and the Mg content of a K-bentonite formed from felsic source magmas commonly is mainly related to the Mg concentration of the sediment porewater (McCarty et al., 2009; Arslan et al., 2010; Clauer et al., 2022). Uptake of Mg^{2+} and K^{+} cations from porewater by K-bentonites is controlled mainly by exchangeable interlayer sites of smectitic clays and illitization of smectite during diagenesis (Göncüoğlu et al., 2016; Huff, 2016; Mills et al., 2023). Therefore, the MgO and K_2O contents of K-bentonites are intimately related to the sedimentary environments in which alteration takes place (Table 1), with relatively higher MgO/K_2O (> 0.30) and MgO/Al_2O_3 (> 0.056) indicative of marine environments, and lower values indicative of lacustrine and paludal terrestrial environments (Hong et al., 2019). The LD-1, LD-2, and CNH-16 K-bentonites yield MgO/K_2O ratios of 0.660, 1.256, 0.780, and MgO/Al_2O_3 ratios of 0.151, 0.292, 0.145, respectively (Table 1), indicative of marine salinity conditions. In contrast, Sample CNH-12 yielded MgO/K_2O of 0.202 and MgO/Al_2O_3 of 0.015, indicative of terrestrial facies (i.e., lacustrine or paludal), similar to those in the TC and ZJ sections (Table 3).

The TiO_2/Al_2O_3 ratios of K-bentonites are inherited from their source rocks, and this proxy has been widely used to probe the origins of epiclastic and terrigenous materials (Hower et al., 2015). For felsic volcanic ashes, TiO_2/Al_2O_3 ratios > 0.140 suggest that the deposits have undergone strong reworking, ratios of 0.055–0.140 indicate weak reworking, and ratios < 0.055 reflect the primary composition of the ash (Hong et al., 2019). In this study, a TiO_2/Al_2O_3 ratio of 0.128 for the CNH-16 K-bentonite indicates strong reworking, ratios of 0.070 and 0.083 for the LD-1 and LD-2 K-bentonites reflect relatively weak reworking or admixture of terrigenous materials, and a ratio of 0.038 for the CNH-12 K-bentonite indicates a primary ash composition with no apparent reworking (Table 3). These inferences of degree of reworking are consistent with the REE distributions of the studied K-bentonites (Fig. 6(a)). The REE profile of the lagoonal CNH K-bentonite (CNH-12) exhibits the similar shape of shallow marine, while those of other K-bentonites (CNH-12, LD-1, LD-2) are similar to those of paludal to terrestrial transitional environments (Hong et al., 2019). In neighboring regions, K-bentonites in paludal and mixed marine-terrestrial environments usually have TiO_2/Al_2O_3 ratios > 0.14 due to strong reworking, and those in lacustrine environments show modified TiO_2/Al_2O_3 ratios of 0.027−0.121 that reflect weak reworking and/or admixture of terrigenous materials (Table 3). K-bentonites in the lower sections of littoral environment generally have TiO_2/Al_2O_3 ratios < 0.055, whereas those in the upper sections have TiO_2/Al_2O_3 ratios > 0.055, suggesting weak modification of ashes in the upper profiles, consistent with the level of reworking of the LD and CNH K-bentonites.

Depositional environmental conditions of K-bentonites are also documented by the morphology of clay minerals. The formation of clay minerals from clearly confined volcanic ash grains and the presence of smectite in the interstitial spaces in the LD K-bentonites indicate an alteration of the primary depositional ash (Figs. 5(a) and 5(b)), and the common presence of well-confined volcanic ash particles is consistent with a littoral depositional environment. The close association of kaolinite with mixed-layer I/S in the CNH-12 K-bentonite strongly suggests that it experienced strong weathering prior to burial diagenesis (Fig. 5(c)), and the face-to-face arrangement of mixed-layer I/S clays in the CNH-16 K-bentonite reflects its relatively slow accumulation rate (Fig. 5(d)). Change in depositional environment of the K-bentonites is also reflected by the morphology of authigenic anatase (Hong et al., 2020, 2022; Liu et al., 2024b; Figs. 5(e)−5(h)). In Sample CNH-12, anatase is present as distinctively anhedral crystals of sponge-like aggregates, suggesting an organic acid-rich environment similar to the porewater chemistry of terrestrial-marine transitional to paludal environments, as the sponge-like aggregates of authigenic anatase involve deposition of Ti associated with organic acids (Schulz et al., 2016; Liu et al., 2019). Similar to Sample LD-1, authigenic anatase in Sample CNH-16 displays distinctively tetragonal bipyramidal to truncated tetragonal bipyramidal shapes, indicating the shallow-marine to nearshore littoral sedimentary environment for formation of the LD-1 and CNH-16 K-bentonites. However, the euhedral tetragonal and short prism morphologies of authigenic anatase in LD-2 ash suggest a phase of basin deepening (Hong et al., 2022), providing evidence of the Early Triassic transgression.

A strong negative Eu anomaly in the REE distributions of felsic igneous rocks is generally attributed to REE fractionation during feldspar precipitation in the source magma chamber (Bea, 1996). During weathering and alteration of ash in seawater, this inherited negative Eu anomaly can be modified by dissolution and recrystallization processes in sediment porewaters (Chen et al., 2015). As a result, the Eu anomaly can be reduced in response to stronger weathering and the effects of diagenesis under oxidizing conditions (MacRae et al., 1992; Püspöki et al., 2008). As shown in Fig. 6, the lack of Eu anomalies in samples LD-1, LD-2, and CNH-16 conform to patterns for K-bentonites deposited in littoral to mixed marine-terrestrial environments, while that of Sample CNH-12 shows a relatively weak Eu anomaly that is similar to those associated with lacustrine facies K-bentonites (Hong et al., 2019). Overall, the weak to missing Eu anomalies of the LD and CNH K-bentonites indicate limited reduction and transport of Eu during weathering and diagenesis under slightly acidic conditions (Murray, 1994).

Except for the presence of mixed-layer kaolinite/smectite (K/S) but absence of mixed-layer I/S clays in K-bentonites of mixed marine-terrestrial facies, K-bentonites of terrestrial lacustrine to marine facies in the Permian-Triassic boundary strata of southwestern China contain mainly highly ordered R1 and R3 mixed-layer I/S clays (Hong et al., 2019). The R1 and R3 I/S clays in the LD and CNH K-bentonites contain 7%−21% and 16%−33% smectite layers, suggesting maximum burial temperatures of 190°C−200°C and 170°C−190°C, respectively (Šucha et al., 1993). K-bentonites deposited in brackish environments (Sr/Ba = 0.25−0.50) usually consist of kaolinite and minor mixed-layer I/S and exhibit strong chemical weathering owing to the acidic and reducing conditions of such facies (Table 3). In contrast, K-bentonites in paludal and marine-terrestrial transitional environments usually experience strong reworking and formed in an open system due to intense chemical leaching. This environment is often acidic and oxic and the mineral compositions of K-bentonites are dominantly kaolinite and minor K/S and mixed-layer I/S clays. The porewater conditions such as redox, salinity, and pH, and the availability of cations are largely different between K-bentonites of lacustrine, paludal and marine-terrestrial transitional, lagoonal, and littoral environments, which result in distinct patterns of chemical weathering and transformation of clay phases and, thus, in the mineralogy and geochemistry of the K-bentonites.

5 Conclusions

K-bentonites in freshwater lacustrine, lagoon, mixed marine-terrestrial, and littoral-neritic facies contain mainly mixed-layer I/S clays, kaolinite and I/S, kaolinite and K/S, and smectite and I/S, respectively. The presence of smectite in K-bentonites suggests a higher seawater pH in littoral-neritic environment due to biological activity and more readily loss of porewater K. The abundant kaolinite in K-bentonites results from strong chemical weathering in an acidic and oxidizing environment characterized by low porewater pH.

The presence of chlorite in the CNH-16 K-bentonite suggests a mixture of detrital chlorite due to condensed sedimentation of terrigenous input during a period of transgression, as confirmed by its high TiO_2/Al_2O_3 ratio (0.128). The TiO_2/Al_2O_3 ratios of 0.070 and 0.083 for the LD-1 and LD-2 K-bentonites reflect relatively weak reworking of these K-bentonites. The TiO_2/Al_2O_3 ratio of 0.038 for the CNH-12 K-bentonite indicates alteration from its primary ash composition with no reworking.

K-bentonites preserve significant information regarding the sedimentary and diagenetic environments of their formation. The LD K-bentonites and their adjacent host sediments, which accumulated in littoral environments, have Sr/Ba ratios of 0.34−0.49, confirming the presence of a low-energy coastal brackish-facies belt in South China during the Permian-Triassic transition, whereas the higher Sr/Ba ratios of the CNH sediments (0.67−1.07) indicate higher salinities in their depositional environment due to a transient interval of aridification and climatic warming.

Competing interests The authors declare that they have no competing interests.

Author Contributions Hanlie Hong: conceptualization, writing (original draft);Xiaoxue Jin, Chen Liu: Formal analysis, investigation and methodology;Thomas J. Algeo: writing (editing).

Data Availability Statement The data sets generated and/or analyzed during the current study are available on request.

Acknowledgments This work was supported by the National Natural Science Foundation of China (Grant Nos. 42472064 and 42172045). The authors also wish to thank Dr. Chu D.L. for assistance in sample collection, Dr. Yu J.S. for help with the XRD analyses, Dr. Jin L. L. for elemental analyses, and especially the three anonymous reviewers for their insightful comments and helpful suggestions.

References

Algeo T J, Hong H L, Wang C W (2025). The chemical index of alteration (CIA) and interpretation of ACNK diagrams. Chem Geol, 671: 122474

Algeo T J, Tribovillard N (2009). Environmental analysis of paleoceanographic systems based on molybdenum–uranium covariation. Chem Geol, 268(3−4): 211–225

Alizai A, Hillier S, Clift P D, Giosan L, Hurst A, VanLaningham S, Macklin M (2012). Clay mineral variations in Holocene terrestrial sediments from the Indus Basin. Quat Res, 77(3): 368–381

Armstrong-Altrin J S, Machain-Castillo M L, Rosales-Hoz L,

Carranza-Edwards A, Sanchez-Cabeza J A, Ruíz-Fernández A C (2015). Provenance and depositional history of continental slope sediments in the Southwestern Gulf of Mexico unraveled by geochemical analysis. Cont Shelf Res, 95: 15–26

Arslan M, Abdiogğlu E, Kadìr S (2010). Mineralogy, geochemistry, and origin of bentonite in Upper Cretaceous pyroclastic units of the Tirebolu area, Gìresun, Northeast Turkey. Clays Clay Miner, 58(1): 120–141

Bau M, Koschinsky A, Dulski P, Hein J R (1996). Comparison of partitioning behaviors of yttrium, rare earth elements, and titanium between hydrogenetic marine ferromanganese crusts and seawater. Geochim Cosmochim Acta, 60(10): 1709–1725

Bea F (1996). Residence of REE, Y, Th and U in granites and crustal protoliths; implications for the chemistry of crustal melt. J Petrol, 37(3): 521–552

Bercovici A, Cui Y, Forel M B, Yu J X, Vajda V (2015). Terrestrial paleoenvironment characterization across the Permian-Triassic boundary in South China. J Asian Earth Sci, 98: 225–246

Bozkaya Ö, Günal-Türkmenoğlu A, Göncüoğlu M C, Ünlüce Ö, Yilmaz İ Ö, Schroeder P A (2016). Illitization of Late Devonian-Early Carboniferous K-bentonites from Western Pontides, NW Turkey: implications for their origin and age. Appl Clay Sci, 134: 257–274

Caballero E, Reyes E, Delgado A, Huertas F, Linares J (1992). The formation of bentonite: mass balance effects. Appl Clay Sci, 6(4): 265–276

Chamley H (1989). Clay Sedimentology. Berlin: Springer, 1–623

Chanu A K, Manikyamba C, Subramanyam K S V, Raza W, Gangula H R (2023). Geochemistry of the Neoarchean Dodguni carbonates of Chitradurga greenstone belt, Dharwar Craton, India: implications on depositional environment. Geol J, 58(2): 648–661

Chen J, Algeo T J, Zhao L, Chen Z Q, Cao L, Zhang L, Li Y (2015). Diagenetic uptake of rare earth elements by bioapatite, with an example from lower Triassic conodonts of South China. Earth Sci Rev, 149: 181–202

Chen Q, Zhang D, Wang J, Zhao F, Liu Y, Zhang Z, Sun X, Huang C, Bai Y (2020). Geochemical characteristics of carbonate rocks in a salinized lacustrine basin: a case study from Oligocene formation in the Qaidam Basin, northwestern China. Carbonates Evaporites, 35(2): 40

Clauer N, Williams L B, Uysal I T (2022). Boron and lithium isotopic signatures of nanometer-sized smectite-rich mixed-layers of bentonite beds from Campos Basin (Brazil). Clays Clay Miner, 70(1): 72–83

Erkoyun H, Kadir S, Külah T, Huggett J (2017). Mineralogy, geochemistry and genesis of clays interlayered coal seams succession in the Neogene lacustrine Seyitömer coal deposit, Kütahya, western Turkey. Int J Coal Geol, 172: 112–133

Fortey N J, Merriman R J, Huff W D (1996). Silurian and Late-Ordovician K-bentonites as a record of late Caledonian volcanism in the British Isles. Trans R Soc Edinb Earth Sci, 86(3): 167–180

Göncüoğlu M C, Günal-Türkmenoğlu A, Bozkaya Ö, Ünlüce-Yücel Ö, Okuyucu C, Yilmaz İ Ö (2016). Geological features and geochemical characteristics of late Devonian–early Carboniferous K-bentonites from northwestern Turkey. Clay Miner, 51(4): 539–562

Gong N N, Hong H L, Huff W D, Fang Q, Bae C J, Wang C W, Yin K, Chen S L (2018). Influences of sedimentary environments and volcanic sources on diagenetic alteration of volcanic tuffs in South China. Sci Rep, 8(1): 7616

He B, Zhong Y T, Xu Y G, Li X H (2014). Triggers of Permo-Triassic boundary mass extinction in South China: the Siberian Traps or Paleo-Tethys ignimbrite flare-up. Lithos, 204: 258–267

Heintz M L, Yancey T E, Miller B V, Heizler M T (2015). Tephrochronology and geochemistry of Eocene and Oligocene volcanic ashes of east and central Texas. Geol Soc Am Bull, 127(5−6): 770–780

Hints R, Kirsimäe K, Somelar P, Kallaste T, Kiipli T (2008). Multiphase Silurian bentonites in the Baltic palaeobasin. Sediment Geol, 209(1−4): 69–79

Hong H L, Algeo T J, Fang Q, Zhao L L, Ji K P, Yin K, Wang C W, Cheng S (2019). Facies dependence of the mineralogy and geochemistry of altered volcanic ash beds: an example from Permian-Triassic transition strata in southwestern China. Earth Sci Rev, 190: 58–88

Hong H L, Fang Q, Zhao L L, Schoepfer S, Wang C W, Gong N N, Li Z, Chen Z Q (2017). Weathering and alteration of volcanic ashes in various depositional settings during the Permian-Triassic transition in South China: mineralogical, elemental and isotopic approaches. Palaeogeogr Palaeoclimatol Palaeoecol, 486: 46–57

Hong H L, Ji K P, Liu C, Algeo T J, Yin K, Zhao L L, Hochella M F, Fang Q, Wang C W (2022). Authigenic anatase nanoparticles as a proxy for sedimentary environment and porewater pH. Am Mineral, 107(12): 2176–2187

Hong H L, Jin X, Wan M, Ji K, Liu C, Algeo T J, Fang Q (2020). Occurrence of anatase in reworking altered ash beds (K-bentonites and tonsteins) and discrimination of source magmas: a case study of terrestrial Permian–Triassic boundary successions in China. Clay Miner, 55(4): 329–341

Hower J C, Eble C F, O'Keefe J M K, Dai S, Wang P, Xie P, Liu J, Ward C R, French D (2015). Petrology, palynology, and geochemistry of Gray Hawk Coal (early Pennsylvanian, Langsettian) in eastern Kentucky, USA. Minerals (Basel), 5(3): 592–622

Huff W D (2016). K-bentonites: a review. Am Mineral, 101(1): 43–70

Isozaki Y, Shimizu N, Yao J, Ji Z, Matsuda T (2007). End-Permian extinction and volcanism-induced environmental stress: the Permian–Triassic boundary interval of lower-slope facies at Chaotian, South China. Palaeogeogr Palaeoclimatol Palaeoecol, 252(1−2): 218–238

Jones B, Manning D A (1994). Comparison of geochemical indices used for the interpretation of palaeoredox conditions in ancient mudstones. Chem Geol, 111(1−4): 111–129

Kasten S, Barker-Jorgensen B (2000). Sulfate reduction in marine sediments. In: Schulz H D, Zabel M, eds. Marine Geochemistry. Berlin: Springer, 263–282

Kiipli T, Kiipli E, Kallaste T, Hints R, Somelar P, Kirsimäe K (2007). Altered volcanic ash as an indicator of marine environment, reflecting pH and sedimentation rate – Example from the Ordovician Kinnekulle bed of Baltoscandia. Clays Clay Miner,

55(2): 177–188

Kramer W, Weatherall G, Offler R (2001). Origin and correlation of tuffs in the Permian Newcastle and Wollombi Coal measures, NSW, Australia, using chemical fingerprinting. Int J Coal Geol, 47(2): 115–135

Kumar R, Hameed R, Tiwari P, Kumar N, Srivastava P (2024). Major, trace and rare earth element geochemistry of Archaean carbonate sediments of Tanwan Group rocks of the Bhilwara Supergroup, India: implications for seawater geochemistry and depositional environment. Carbonates Evaporites, 39(2): 14

Lei H Y, Wang L, Zhang W D, Jiang M J, Bo Y, Fang Q F (2022). Impact of environmental acidity on the geomechanical and mineralogical behavior of marine clay. Bull Eng Geol Environ, 81(1): 35

Liao Z, Hu W, Cao J, Wang X, Yao S, Wu H, Wan Y (2016). Heterogeneous volcanism across the Permian–Triassic Boundary in South China and implications for the Latest Permian Mass Extinction: new evidence from volcanic ash layers in the Lower Yangtze Region. J Asian Earth Sci, 127: 197–210

Liu C, Fang Q, Hong H L, Song Q, Ji K, Gong N, Shen X, Algeo T J (2024b). Illitization of smectite influenced by chemical weathering and its potential control of anatase formation in altered volcanic ashes. Am Mineral, 109(10): 1691–1704

Liu L, Liu H, Zhang C, Zhang J, Zhai X, Guan N, Wang Z, Liu Q (2024a). Late Carboniferous marine-continental transitional sediments in the Datong Basin, North China: mineralogical and geochemical characteristics and paleoenvironmental significance. Mar Pet Geol, 162: 106714

Liu L, Zhang H, Algeo T J, Zhang K N, Hong H L, Zhang S, Liu Q (2021). Control of coal-bearing claystone composition by sea level and redox conditions: an example from the Upper Paleozoic of the Datong Basin, North China. Appl Clay Sci, 211: 106204

Liu Z R R, Zhou M F, Williams-Jones A E, Wang W, Gao J F (2019). Diagenetic mobilization of Ti and formation of brookite/anatase in early Cambrian black shales, South China. Chem Geol, 506: 79–96

MacRae N D, Nesbitt H W, Kronberg B I (1992). Development of a positive Eu anomaly during diagenesis. Earth Planet Sci Lett, 109(3−4): 585–591

McCarty D K, Sakharov B A, Drits V A (2009). New insights into smectite illitization: a zoned K-bentonite revisited. Am Mineral, 94(11−12): 1653–1671

McLennan S M (1989). Rare earth elements in sedimentary rocks: influence of provenance and sedimentary processes. Rev Mineral Geochem, 21(1): 169–200

McLennan S M (2001). Relationships between the trace element composition of sedimentary rocks and upper continental crust. Geochemistry Geophysics Geosystems, 2: 2000GC000109

Mills M M, Sanchez A C, Boisvert L, Payne C B, Ho T A, Wang Y F (2023). Understanding smectite to illite transformation at elevated (>100 °C) temperature: effects of liquid/solid ratio, interlayer cation, solution chemistry and reaction time. Chem Geol, 615: 121214

Mitchell C E, Goldman D, Delano J W, Samson S D, Bergström S M (1994). Temporal and spatial distribution of biozones and facies relative to geochemically correlated K-bentonites in the Middle Ordovician Taconic foredeep. Geology, 22(8): 715–718

Murray R W (1994). Chemical-criteria to identify the depositional environment of chert-general-principles and applications. Sediment Geol, 90(3−4): 213–232

Nechaev V P, Dai S, Chekryzhov I Y, Tarasenko I A, Zin'kov A V, Moore T A (2022). Origin of the tuff parting and associated enrichments of Zr, REY, redox-sensitive and other elements in the Early Miocene coal of the Siniy Utyes Basin, southwestern Primorye, Russia. Int J Coal Geol, 250: 103913

Nesbitt H W, Markovics G (1997). Weathering of granodioritic crust, long-term storage of elements in weathering profiles, and petrogenesis of siliciclastic sediments. Geochim Cosmochim Acta, 61(8): 1653–1670

Nesbitt H W, Young G M (1982). Early Proterozoic climates and plate motions inferred from major element chemistry of lutites. Nature, 299(5885): 715–717

Núñez M A, Recio J M (2007). Kaolinitic paleosols in the south west of the Iberian Peninsula (Sierra Morena region, Spain). Paleoenvironmental implications. Catena, 70(3): 388–395

Osacký M, Bai Y, Uhlík P, Pálková H, Caplovicová M (2023). Mineralogy, chemistry, and thermal and surface properties of various technological types of K-bentonite from the Dolna Ves deposit (Kremnicke Vrchy Mts. , Western Carpathians, Slovakia). Clays Clay Miner, 71(6): 650-672

Peng Y Q, Zhang S X, Yu T X, Yang F Q, Gao Y Q, Shi G R (2005). High-resolution terrestrial Permian–Triassic eventostratigraphic boundary in western Guizhou and eastern Yunnan, southwestern China. Palaeogeogr Palaeoclimatol Palaeoecol, 215(3−4): 285–295

Pillai S S K, Manoj M C, Mathews R P, Murthy S, Sahoo M, Saxena A, Sharma A, Pradhan S, Kumar S (2023). Lower Permian Gondwana sequence of Rajhara (Daltonganj Coalfield), Damodar Basin, India: floristic and geochemical records and their implications on marine ingressions and depositional environment. Environ Geochem Health, 45(10): 6923–6953

Püspöki Z, Kozák M, Kovács-Pálffy P, Szepesi J, McIntosh R, Kónya P, Vincze L, Gyula G (2008). Geochemical records of a bentonitic acid-tuff succession related to a transgressive systems tract – indication of changes in the volcanic sedimentation rate. Clays Clay Miner, 56(1): 23–38

Renock D, Landis J D, Sharma M (2016). Reductive weathering of black shale and release of barium during hydraulic fracturing. Appl Geochem, 65: 73–86

Reynolds R C Jr, Reynolds R C III (1996). NEWMOD for Windows. The Calculation of One-dimensional X-ray Diffraction Patterns of Mixed-layered Clay Mineral. Hanover: New Hampshire

Schulz H, Wirth R, Schreiber A (2016). Nanocrystal formation of TiO_2 polymorphs brookite and anatase due to organic-inorganic rock-fluid interactions. J Sediment Res, 86(2): 59–72

Sheldon N D, Tabor N J (2009). Quantitative paleoenvironmental and paleoclimatic reconstruction using paleosols. Earth Sci Rev, 95(1−2): 1–52

Shen M, Dai S, Graham I T, Nechaev V P, French D, Zhao F, Shao L, Liu S, Zuo J, Zhao J, Chen K, Xie X (2021). Mineralogical and geochemical characteristics of altered volcanic ashes (tonsteins and K-bentonites) from the latest Permian coal-bearing strata of western

Guizhou Province, southwestern China. Int J Coal Geol, 237: 103707

Shu W (2022). Permian–Triassic Floral Successions—Fossil Evidence from North China, South China and Xinjiang. Dissertation for Doctor Degree. Wuhan: China University of Geosciences-Wuhan

Somelar P, Kirsimäe K, Hints R, Kirs J (2010). Illitization of Early Paleozoic K-bentonites in the Baltic Basin: decoupling of burial- and fluid-driven processes. Clays Clay Miner, 58(3): 388–398

Song Q, Hong H L, Algeo T J, Fang Q, Zhao C L, Liu C, Xu Y X (2023). Clay mineralogy mediated by pH and chemical weathering intensity of Permian–Triassic boundary K-bentonites at Dongpan (Guangxi, South China). Chem Geol, 617: 121262

Song T, Tong J, Tian L, Chu D, Huang Y (2019). Taxonomic and ecological variations of Permian-Triassic transitional bivalve communities from the littoral clastic facies in southwestern China. Palaeogeogr Palaeoclimatol Palaeoecol, 519: 108–123

Stampfli G M, Borel G D (2002). A plate tectonic model for the Paleozoic and Mesozoic constrained by dynamic plate boundaries and restored synthetic oceanic isochrons. Earth Planet Sci Lett, 196(1−2): 17–33

Šucha V, Kraust I, Gerthofferová H, Peteš J, Sereková M (1993). Smectite to illite conversion in bentonites and shales of the East Slovak Basin. Clay Miner, 28(2): 243–253

Thorpe C L, Lloyd J L, Law G T W, Burke L T, Shaw S, Bryan N D, Morris K (2012). Strontium sorption and precipitation behaviour during bioreduction in nitrate impacted sediments. Chem Geol, 306–307: 114–122

Toulkeridis T, Clauer N, Chaudhuri S, Goldstein S L (1998). Multimethod (K-Ar, Rb-Sr, Sm-Nd) dating of bentonite minerals from the eastern United States. Basin Res, 10(2): 261–270

Ver Straeten C A (2008). Volcanic tephra bed formation and condensation processes: a review and examination from Devonian stratigraphic sequences. J Geol, 116(6): 545–557

Wang A, Wang Z, Liu J, Xu N, Li H (2021). The Sr/Ba ratio response to salinity in clastic sediments of the Yangtze River Delta. Chem Geol, 559: 119923

Wei W, Algeo T J (2020). Elemental proxies for paleosalinity analysis of ancient shales and mudrocks. Geochim Cosmochim Acta, 287: 341–366

Wignall P B, Chu D, Hilton J M, Dal Corso J, Wu Y, Wang Y, Atkinson J, Tong J (2020). Death in the shallows: the record of Permo-Triassic mass extinction in paralic settings, southwest China. Global Planet Change, 189: 103176

Wu Y Y, Chu D, Tong J, Song H, Dal Corso J, Wignall P B, Song H, Du Y, Cui Y (2021). Six-fold increase of atmospheric pCO_2 during the Permian–Triassic mass extinction. Nat Commun, 12(1): 2137

Yin H F, Jiang H S, Xia W C, Feng Q L, Zhang N, Shen J (2014). The end-Permian regression in South China and its implication on mass extinction. Earth Sci Rev, 137: 19–33